Supplementary Information (SI) for EES Batteries.
This journal is © The Royal Society of Chemistry 2026

Breaking Solvation Compactness: Methyl Acetate Cosolvent Engineering Enables High-voltage Lithium Metal Batteries at Low Temperatures

Hui Tian,[a] Yufeng Luo,[b] Zixin Hong,[a] Zhenhan Fang,[a] Hengcai Wu,[a] Fei Zhao,[a] Guoqiang Tan,[b] Qunqing Li,[a, c] Shoushan Fan,[a] and Jiaping Wang*[a, c]*

[a] H. Tian, Z. X. Hong, Dr. Z. H. Fang, H. C. Wu, F. Zhao, Prof. Q. Q. Li, Prof. S. S. Fan, Prof. J. P. Wang
Department of Physics and Tsinghua-Foxconn Nanotechnology Research Center, Tsinghua University
Beijing, 100084, China
E-mail: jpwang@tsinghua.edu.cn (Jiaping Wang)

[b] Prof. Y. F. Luo, Prof. G. Q. Tan,
School of Materials Science and Engineering, Beijing Institute of Technology
Beijing 100081, PR China
E-mail: luoyf@bit.edu.cn (Yufeng Luo)

[c] Prof. Q. Q. Li, Prof. J. P. Wang
Department Frontier Science Center for Quantum Information
Beijing, 100084, China

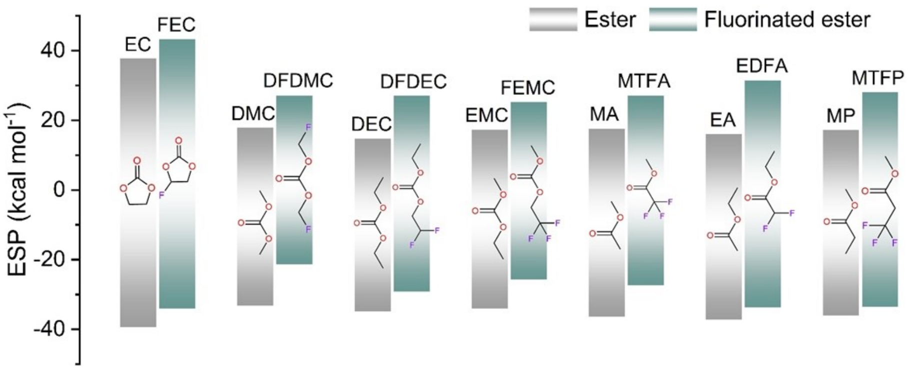

Figure S1. Comparison of density functional theory (DFT)-computed electrostatic potential (ESP) extrema for common carbonate esters, carboxylate esters, and their fluorinated derivatives.

ESP analysis and visualization were implemented using Multiwfn software combined with Visual Molecular Dynamics (VMD) [1–3].

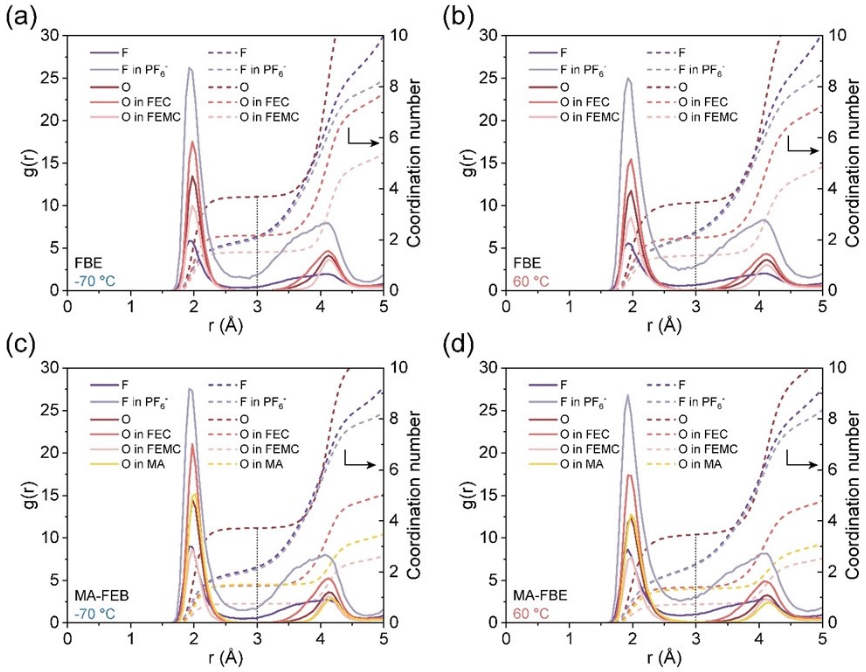

Figure S2. RDFs and CNs of the FBE electrolyte at (a) -70 °C and (b) 60 °C, and the MA-FBE electrolyte at (c) -70 °C and (d) 60 °C.

RDFs within the Forcite module of Materials Studio were calculated for Li^+ and CNs were then determined through integration of the RDF:

$$CN(r) = \int_0^r 4\pi r^2 \rho g(r) dr \approx \sum_{i=0}^{N} 4\pi r_i^2 \rho g(r_i) \Delta r \# (\text{Equation S1})$$

where r denotes the interatomic distance between the central lithium ion (Li^+) and neighboring atoms, N represents the total number of atoms, ρ represents the atomic number density of the system.

The FBE electrolyte was prepared by dissolving 1 M lithium hexafluorophosphate ($LiPF_6$) in a binary solvent mixture of methyl (3,3,3-trifluoroethyl) carbonate (FEMC) and fluoroethylene carbonate ( ) (2:1, v/v). The MA-FBE electrolyte was synthesized by dissolving 1 M $LiPF_6$ in a ternary solvent mixture comprising FEC, FEMC, and methyl acetate (MA) (4:2:4, v/v).

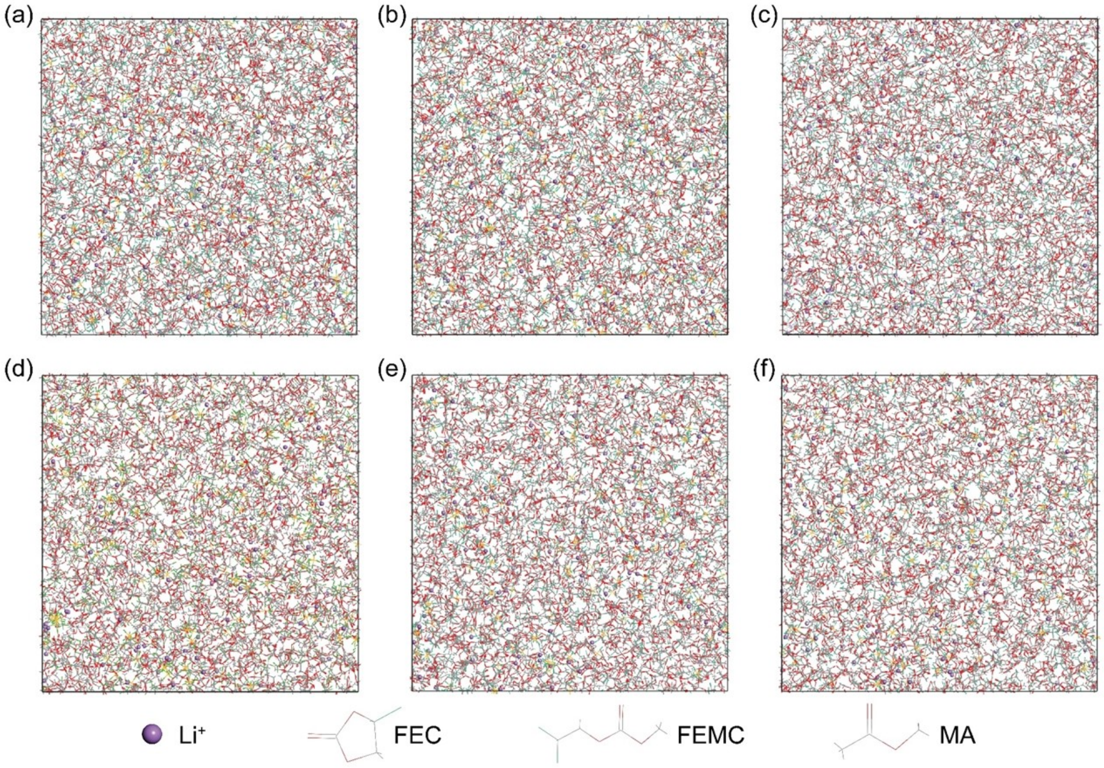

Figure S3. Molecular dynamics (MD) simulation snapshots of the FBE electrolyte at (a) -70 °C, (b) 25 °C and (c) 60 °C, and the MA-FBE electrolyte at (d) -70 °C, (e) 25 °C and (f) 60 °C.

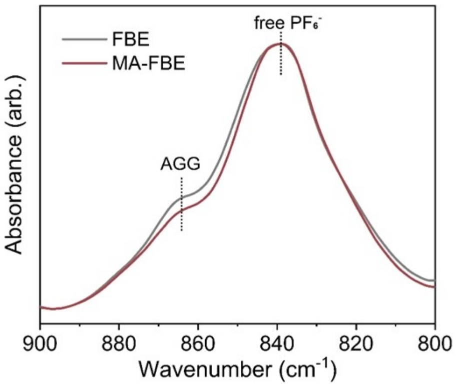

Figure S4. Attenuated total reflectance-Fourier transform infrared spectroscopy (ATR-FTIR) spectra of the FBE and MA-FBE electrolytes.

ATR-FTIR measurements were performed on a Thermo Fisher Scientific Nicolet iS50 spectrometer equipped with a diamond ATR accessory. The ATR-FTIR spectra revealed P-F stretching bands of PF_6^- in the 800-900 cm^{-1} region. The peak near 840 cm^{-1} corresponds to free PF_6^-, while the 870 cm^{-1} feature arises from Li^+-coordinated PF_6^-. The significantly enhanced intensity of the 870 cm^{-1} band in the FBE electrolyte (relative to the MA-FBE electrolyte) provided direct spectroscopic evidence for the presence of ion-aggregated solvation clusters in the FBE electrolyte. [4,5] Integrated computational and experimental results verify the spatially uniform dispersion of solvation structures in the MA-FBE electrolyte.

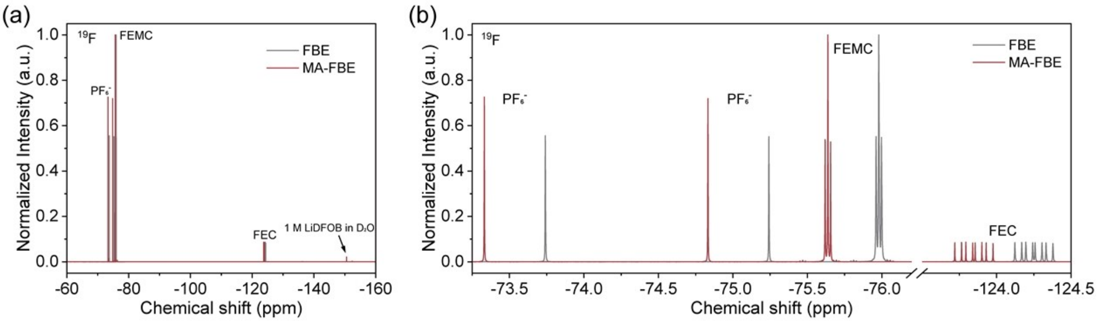

Figure S5. ^{19}F nuclear magnetic resonance (NMR) of the FBE and MA-FBE electrolytes.

The ^{19}F chemical shifts were externally referenced using a coaxial NMR insert filled with 1 M lithium difluoro(oxalato)borate (LiDFOB) in deuterated water (D_2O). Compared with the FBE electrolyte, the characteristic doublet of the PF_6^- anion, multiplet of FEC, and FEMC in MA-FBE all exhibit downfield shifts, with values of 0.41 ppm, 0.34 ppm, and 0.40 ppm, respectively. The observed synchronous downfield shifts of all fluorine-containing species in MA-FBE are in full agreement with the ^7Li NMR results, further validating MA's regulation effect on the electrolyte solvation structure. In FBE, PF_6^- forms multi-directional bridging interactions with multiple Li^+ in compact large ionic clusters, which enhances the nuclear shielding effect of F atoms and results in upfield chemical shifts; FEC and FEMC trapped in the tight solvation structure also exhibit upfield signals due to the high electron cloud density around their F nuclei. The introduction of MA breaks up these large ionic clusters via its weak repulsion and high mobility, converting PF_6^- from a multi-Li^+ bound state to a weakly bound contact ion pairs (CIP) state with a single Li^+. The electron cloud around the F nuclei is polarized under the unidirectional electrostatic attraction of a single Li^+, leading to a significant decrease in the effective electron cloud density and weakened shielding effect, which drives the downfield shift of the characteristic PF_6^- signal. Meanwhile, the accelerated dynamic exchange of solvation structures further amplifies the contribution of weakly bound species to the average chemical shift, leading to the synchronous downfield shift of all fluorine-containing species.

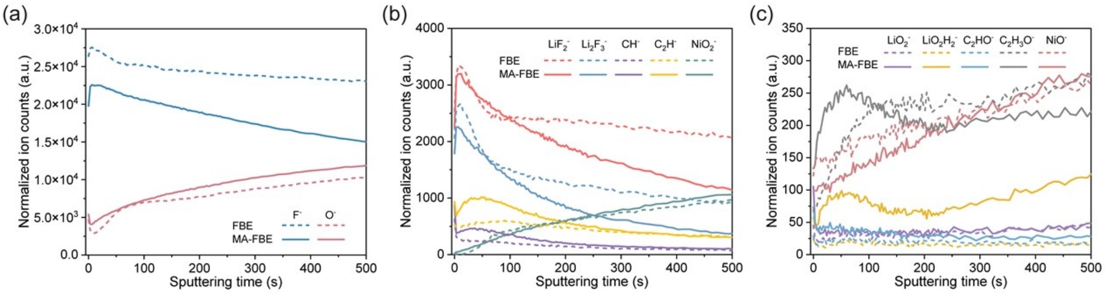

Figure S6. Depth profiles of key negative ion fragments from Time-of-flight secondary ion mass spectrometry (ToF-SIMS) characterization for the CEI on NCM811 cathodes with the FBE and MA-FBE electrolytes. All ion signals are normalized by the formula: normalized counts = (target ion counts / total ion counts of the same depth point) × 10^5. The sputtering direction is from the outer surface of the CEI to the bulk of the NCM811 cathodes.

ToF-SIMS characterizations were performed on a PHI nano TOF II instrument (ULVAC-PHI, Japan) to investigate the chemical composition and vertical distribution of the CEI on cycled NCM811 cathodes. All measurements were carried out in negative ion mode with a 30 keV Bi_3^+ liquid metal ion gun (LMIG) as the primary analysis beam (analysis area: 100 μm × 100 μm), and a 4 kV Ar^+ sputtering beam (200 nA, sputtering area: 400 μm × 400 μm) was used for depth profiling. The sputtering rate was calibrated as 1.0 nm s^{-1} using a standard thermally oxidized SiO_2 wafer.

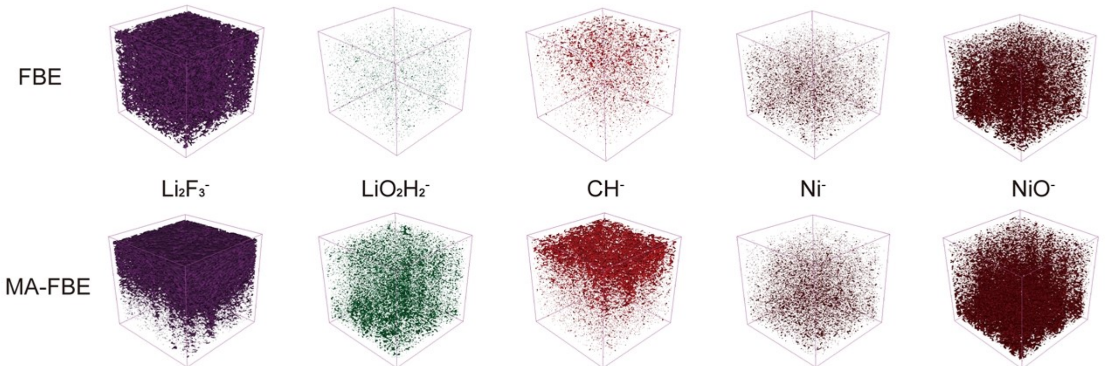

Figure S7. 3D ToF-SIMS chemical reconstruction images of additional key CEI components on the cycled NCM811 cathodes.

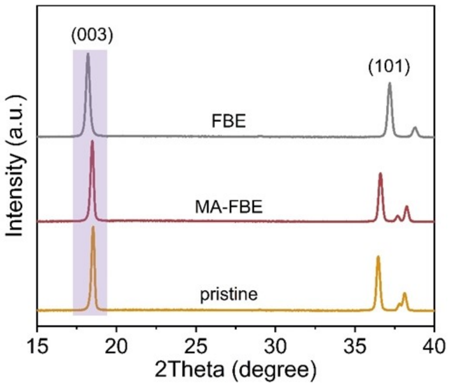

Figure S8. X-ray diffraction (XRD) patterns of pristine $LiNi_{0.8}Mn_{0.1}Co_{0.1}O_2$ (NCM811) cathode and post-electrochemical cycling samples in the FBE and MA-FBE electrolyte systems.

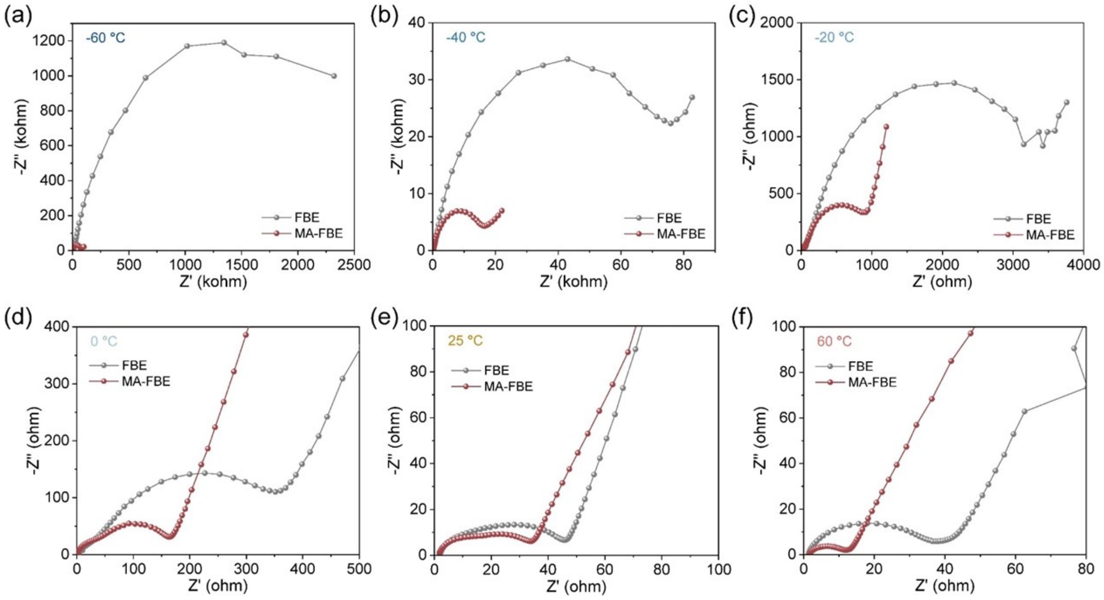

Figure S9. Electrochemical impedance spectroscopy (EIS) of NCM811||Li half cells with the FBE and MA-FBE electrolytes at -60 °C, -40 °C, -20 °C, 0 °C, 25 °C and 60 °C.

The E_a of the charge transfer and Li^+ transport in cathode-electrolyte interphase (CEI) processes was obtained according to the Arrhenius equation:

$$\frac{1}{R_{(ct,\ CEI)}} = Ae^{-\frac{E_a}{RT}}\#(\text{Equation S3})$$

where $R_{(ct,\ CEI)}$ is the charge transfer resistance or the Li^+ transport resistance in CEI, A is the pre-exponential constant, R is the gas constant (8.314 J mol^{-1} K^{-1}), T is the absolute temperature.

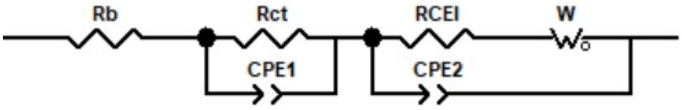

Figure S10. Equivalent circuit diagram for the EIS analysis.

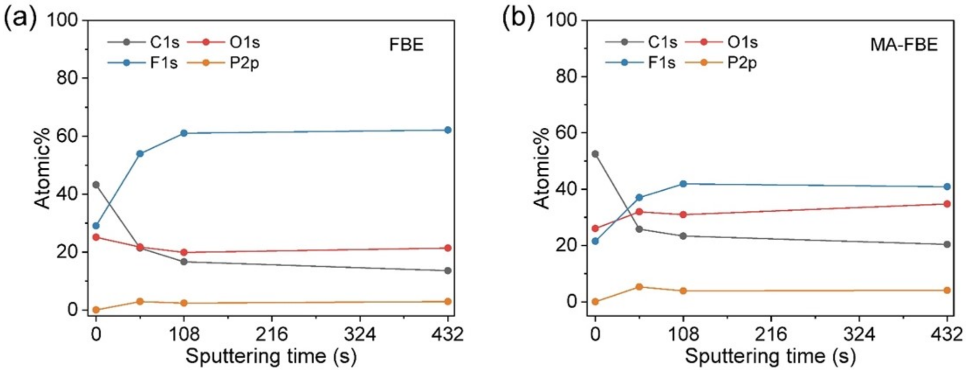

Figure S11. X-ray photoelectron spectroscopy (XPS) general spectra of the solid electrolyte interphase (SEI) on cycled-Li anodes for the (a) FBE and (b) MA-FBE electrolytes.

The NCM811 cathode and Li metal anode samples analyzed by XPS were harvested from NCM811||Li coin cells following 50 electrochemical cycles conducted in distinct electrolyte formulations under standardized conditions: 5 C charge/discharge rate, 3.0-4.8 V voltage window, and 25 °C ambient temperature. All binding energy values were referenced to the C 1s hydrocarbon peak (C-C/C-H) at 284.8 eV for spectral calibration. Sum spectra revealed significantly higher fluoride (F) content in FBE-derived SEI compared to MA-FBE, alongside reduced carbon (C) and oxygen (O) levels, confirming MA-induced organic enrichment.

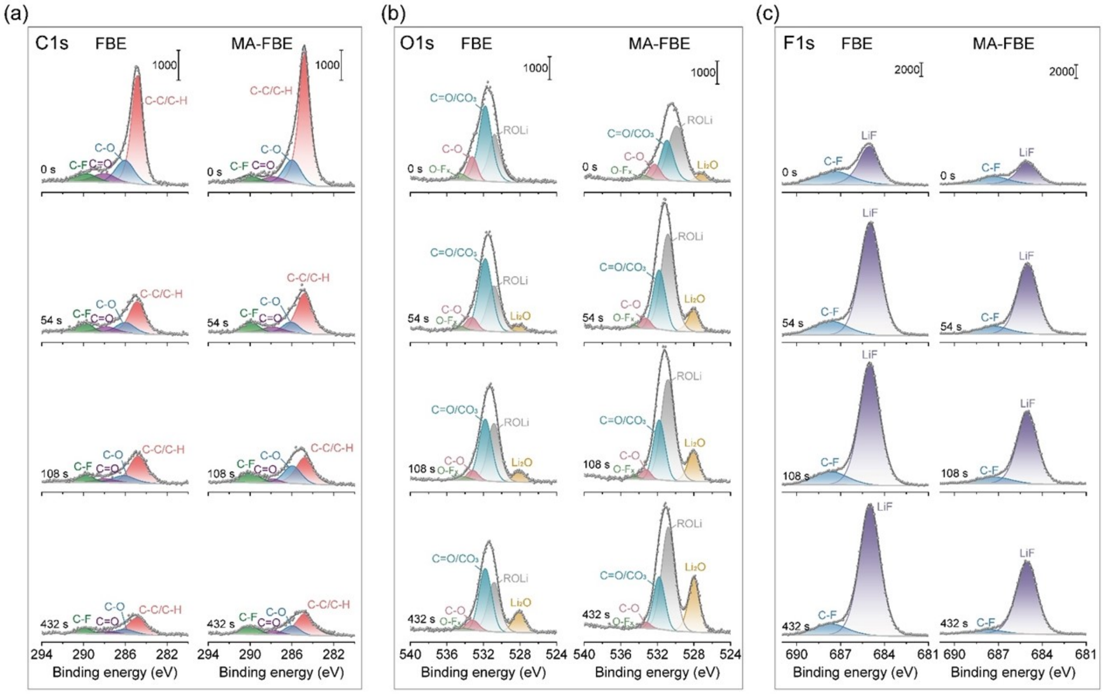

Figure S12. XPS (a) C1s, (b) O1s, and (c) F1s spectra of the SEI.

High-resolution C 1s, O 1s, and F 1s spectra identified C-C/C-H, C-O, C=O, ROLi, and C-F bonds, corresponding to organic components including lithium alkoxides, alkyl carbonates, and fluorinated organics, all derived from the reductive decomposition of MA, FEC, and FEMC. [6,7] Notably, FBE SEI contained excessive LiF, while MA-FBE exhibited enriched organics and Li_2O. Overly inorganic-dominated SEI, exemplified by LiF-rich interphases, increases brittleness, failing to accommodate volume changes during Li cycling, thereby triggering SEI fracture and parasitic reactions that degrade CE. [8] In contrast, the MA-FBE electrolyte enables the formation of a hybrid organic-inorganic SEI architecture. Inorganic components (LiF, Li_2O) provide mechanical rigidity, while organic species confer elasticity to accommodate volume fluctuations during Li cycling. Particularly, Li_2O formed on Li foil enables uniform and rapid Li^+ flux compared to LiF, [9] establishing a critical foundation for stable LMB operation under extreme conditions including wide temperature ranges and high rates. This synergistic SEI composition directly supports the observed improvements in cycling stability and electrochemical reversibility.

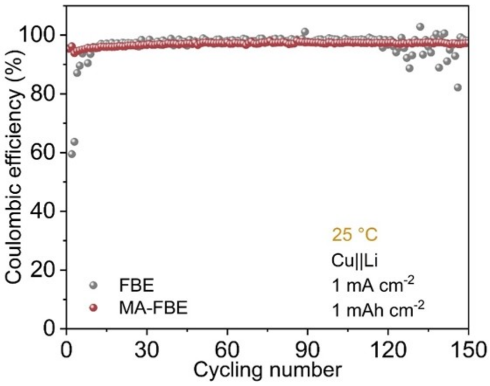

Figure S13. Cycling performance of copper (Cu)||Li cells with the FBE and MA-FBE electrolytes at 25 °C.

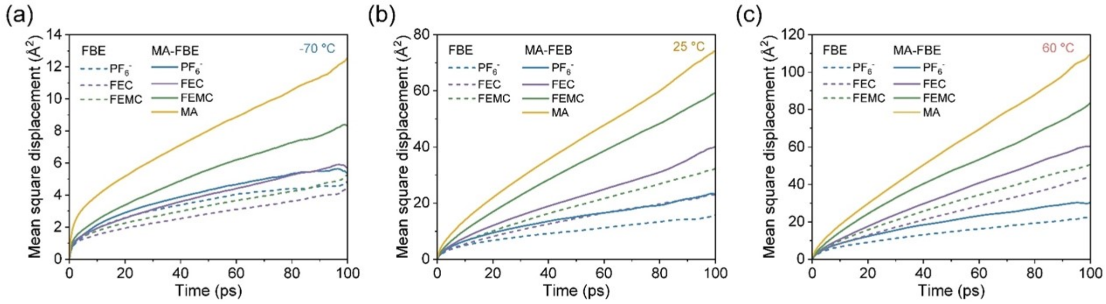

Figure S14. Mean squared displacement (MSD) curves of PF$_6^-$, FEC, FENC, and MA as a function of simulation time in the FBE and MA-FBE electrolytes at (a) -70 °C, (b) 25 °C and (c) 60 °C.

The MSD was calculated using the Forcite module in Materials Studio. A relatively stable segment of the MSD curve with minimal statistical error was selected for linear fitting. Subsequently, the diffusion coefficients (D) of each component in the electrolyte were further determined based on the Einstein relation [10,11], which is expressed as:

$$D = \lim_{t \to \infty} \frac{\langle \Delta r^2(t) \rangle}{6t} = \frac{MSD(t)}{6t} \# (\text{Equation S2})$$

where $\langle \Delta r^2(t) \rangle$ denotes the mean squared displacement over time interval t.

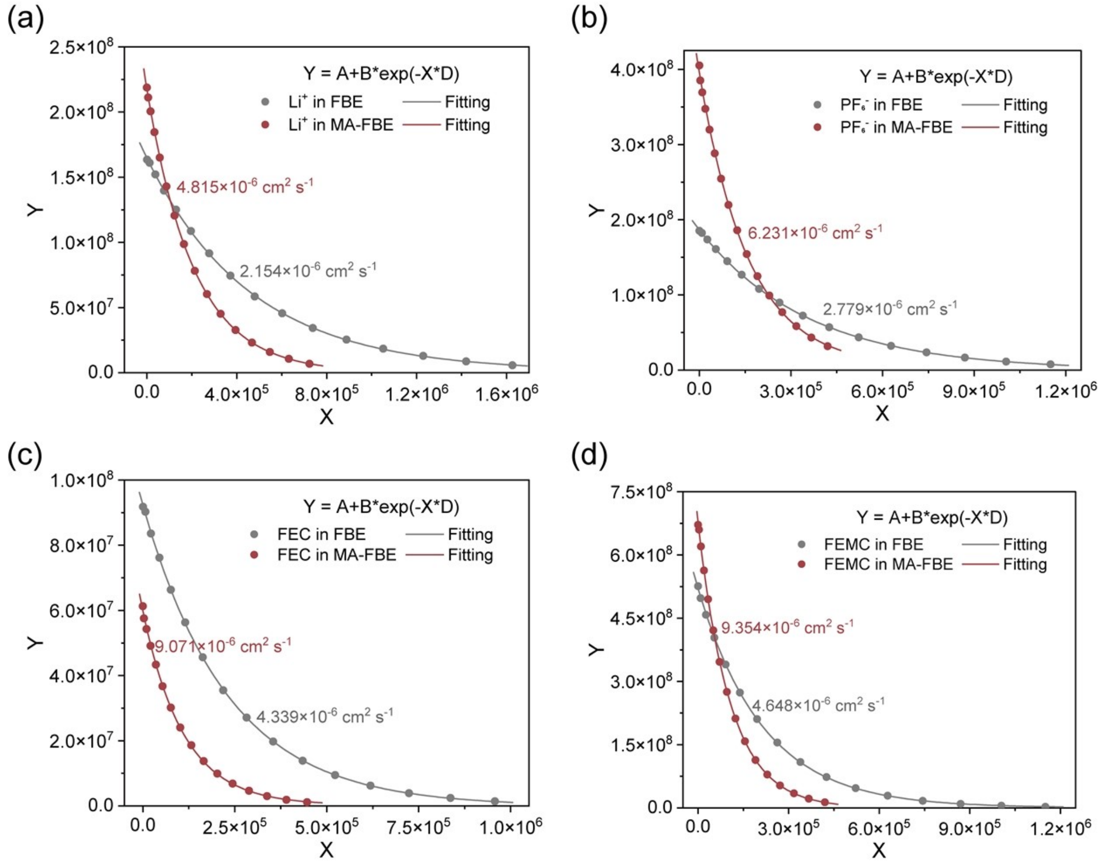

Figure S15. (a) ^{7}Li diffusion-ordered spectroscopy (DOSY) attenuation curves for Li^+ in FBE and MA-FBE electrolytes; ^{19}F DOSY attenuation curves for (b) PF_6^-, (c) FEC and (d) FEMC in FBE and MA-FBE electrolytes.

^{7}Li and ^{19}F chemical shifts were externally referenced using coaxial NMR inserts: ^{7}Li with 1 M lithium chloride (LiCl) in D_2O and ^{19}F with 1 M lithium LiDFOB in D_2O, following independent standardization procedures to avoid sample interference.

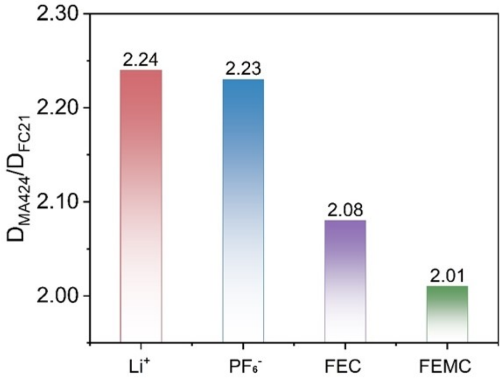

Figure S16. Comparative ratios of D values for individual components (Li^+, PF_6^-, FEC, FEMC) between the MA-FBE and FBE electrolytes via DOSY.

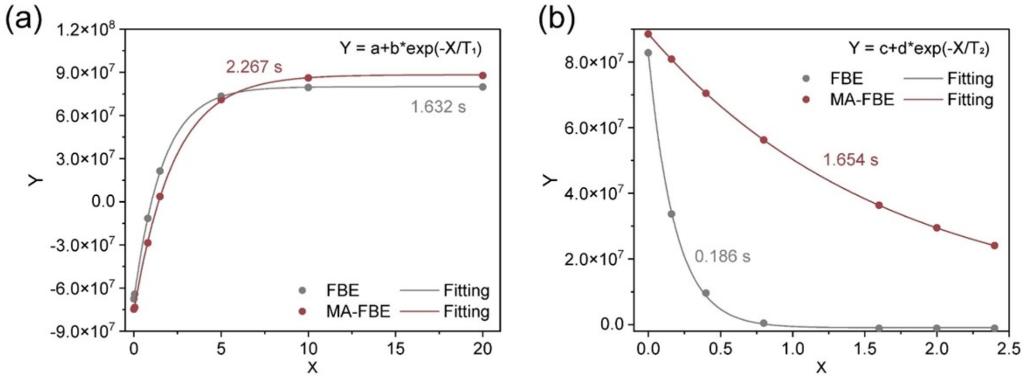

Figure S17. Longitudinal (T_1) and transverse (T_2) relaxation times of FBE and MA-FBE electrolytes measured by ^7Li NMR.

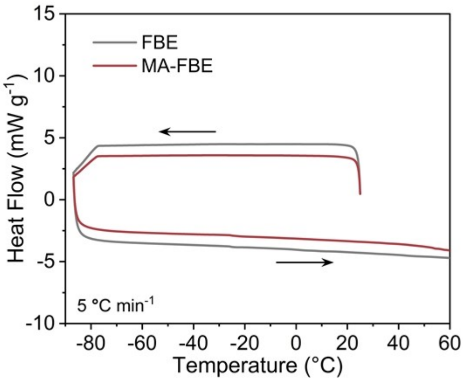

Figure S18. Differential scanning calorimetry (DSC) analysis of the FBE and MA-FBE electrolytes.

DSC measurements were conducted on a TA Instruments Q5000IR analyzer under a nitrogen atmosphere and performed using a two-stage temperature program: a cooling scan from 25.0 °C to -80.0 °C followed immediately by a heating scan to 60.0 °C, both at a constant scanning rate of 5.0 °C min^{-1}. Both electrolytes maintain in the liquid phase across the temperature range of -80 °C to 60 °C.

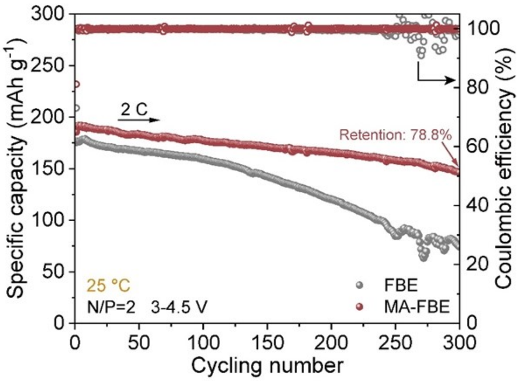

Figure S19. Electrochemical cycling performance of NCM811||Li full cells (3-4.5 V, N/P=2) with the FBE, and MA-FBE electrolytes at 2 C and 25 °C.

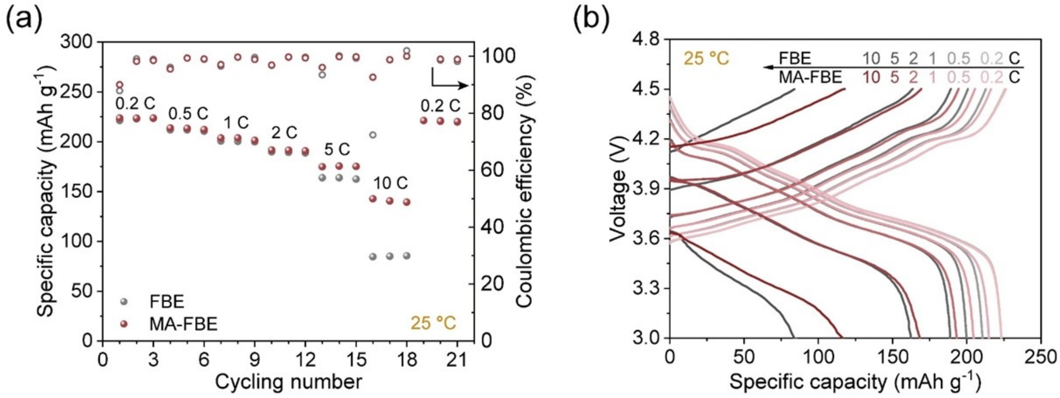

Figure S20. (a) Rate performance and (b) corresponding specific capacity-voltage curves of NCM811||Li cells with the FBE and MA-FBE electrolytes at 25 °C.

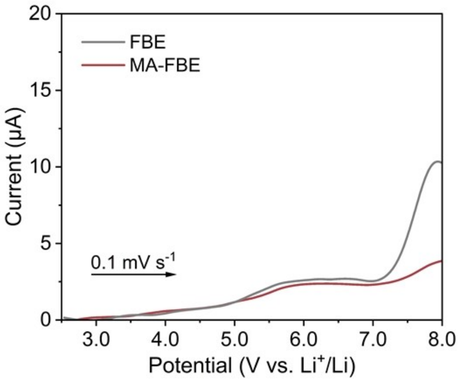

Figure S21. Linear sweep voltammetry (LSV) curves of the FBE and MA-FBE electrolytes.

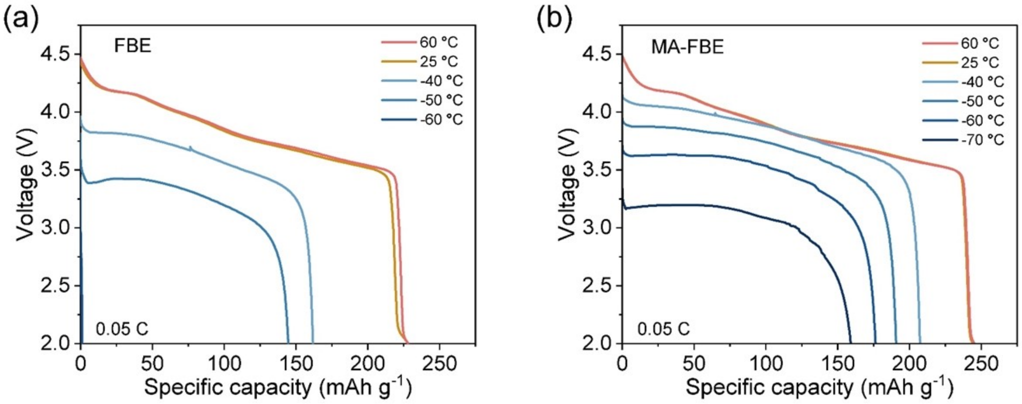

Figure S22. Specific capacity-voltage curves for cells with the (a) FBE and (b) MA-FBE electrolytes charged at RT at 0.5 C and discharged at 60, 25, -40, -50, -60, and -70 °C at 0.05 C.

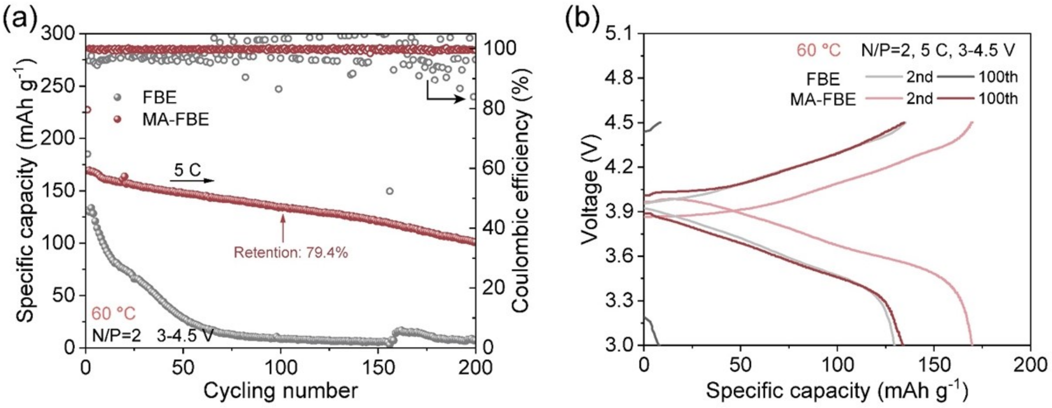

Figure S23. (a) Electrochemical cycling performance and (b) corresponding specific capacity-voltage curves of NCM811||Li full cells with the FBE and MA-FBE electrolytes at 5 C and 60 °C.

Table S1. Comparison of different physical parameters of various organic solvents. [12-22]

Solvents	Melting point (°C)	Boiling point (°C)	Viscosity (mPa s)	Dielectric constants	LUMO (eV)	HOMO (eV)	ESP_{min} (kcal mol^{-1})	ESP_{max} (kcal mol^{-1})
EC	36.4	248	1.90	89.8	-0.6038	-8.4674	-39.460	37.904
FEC	20	210	4.40	79.7	-0.6416	-8.9719	-34.092	43.400
DMC	4	90	0.59	3.1	-0.2348	-8.2135	-33.267	18.147
DFDMC	N/A	120	N/A	N/A	-0.4487	-9.0440	-21.359	27.331
DEC	-43	126	0.75	2.8	-0.2678	-8.0543	-35.009	14.960
DFDEC	N/A	N/A	N/A	N/A	-0.3796	-8.5261	-29.179	27.254
EMC	-53	110	0.65	3.0	-0.2555	-8.1324	-34.166	17.498
FEMC	N/A	74	N/A	9.5	-0.4087	-8.7621	-25.811	25.355
MA	-98	57	0.37	7.3	-0.2748	-7.7893	-36.443	17.796
MTFA	-78	43	N/A	N/A	-1.4343	-8.9117	-27.372	27.293
EA	-84	77	0.46	6.4	-0.3048	-7.6964	-37.304	16.306
EDFA	N/A	N/A	N/A	N/A	-1.1432	-8.4034	-33.827	31.662
MP	-88	80	0.50	6.1	-0.2942	-7.7561	-36.147	17.354
MTFP	N/A	72	N/A	N/A	-0.6631	-8.4094	-33.616	28.216
PC	-49	242	2.50	64.6	-0.6150	-8.3768	-40.538	36.391
PA	-93	101	0.59	6.0	-0.2985	-7.6801	-37.533	16.143
EP	-74	99	0.90	5.7	-0.3102	-7.6652	-36.976	14.727
PP	-80	98	0.68	4.7	-0.3072	-7.6499	-37.188	14.012
DOL	-95	74	0.54	7.3	-0.2667	-7.3-FBE	-31.208	21.139
DME	-58	85	0.46	7.2	-0.1820	-7.1863	-29.978	11.986
AN	-45	82	0.38	36.0	-0.5682	-9.2660	-39.066	27.831
TMP	-46	197	1.70	20.6	-0.3551	-8.2086	-44.349	17.218
DMSO	18	189	1.99	46.4	-0.4664	-6.4886	-48.807	29.852
DMMS	-108	65	0.70	3.7	-0.4337	-7.3721	-42.922	19.248

Note:

The following lists the full names of the reagents mentioned in the table:

Ethylene carbonate (EC)

Fluoroethylene carbonate (FEC)

Dimethyl carbonate (DMC)

Dimethyl difluorocarbonate (DFDMC)

Diethyl carbonate (DEC)

2,2-Difluoroethyl ethyl carbonate (DFDEC)

Ethyl methyl carbonate (EMC)

3,3,3-Fluoroethylmethyl carbonate (FEMC)

Methyl acetate (MA)
Methyltrifluoroacetate (MTFA)
Ethyl acetate (EA)
Ethyl difluoroacetate (EDFA)
Methyl propanoate (MP)
Methyl 3,3,3-trifluoropionate (MTFP)
Propylene carbonate (PC)
Propyl acetate (PA)
Ethyl propionate (EP)
Propyl phenylacetate (PP)
1,3-Dioxolane (DOL)
Dimethoxyethane (DME)
Acetonitrile (AN)
Trimethyl phosphate (TMP)
Dimethyl sulfoxide (DMSO)
Dimethyldimethoxysilane (DMMS)

Table S2. XRD parameter analysis of pristine and cycled NCM811 cathodes in different electrolyte systems.

	pristine	FBE	MA-FBE
$2\theta_{003}$ (°)	18.519	18.209	18.480
d_{003} (Å)	4.787	4.863	4.795
$FWHM_{003}$(°)	0.212	0.277	0.218
$2\theta_{101}$ (°)	36.436	37.191	36.575
d_{101} (Å)	2.464	2.416	2.455
$FWHM_{101}$(°)	0.211	0.274	0.214
c (Å)	14.361	14.589	14.385
a (Å)	2.888	2.827	2.877
c/a	4.973	5.161	5.000

Table S3. Advanced electrolytes for lithium metal batteries: comprehensive performance summary at high-voltage, low-temperature, and high-temperature conditions.

Refs.	Electrolyte formula	Cell type	High-voltage performance at RT	Capacity over RT capacity at LT	Performance at HT
23	LiFSI/DME/TTE (1:1:3 by mol.)	LCO‖Li (450 μm)	4.55 V 87.6%@200 cycles, N/P=35.7	-30 °C 88%@0.15 C (charged at RT)	55 °C 81.3%@200 cycles, 0.24 C/0.73 C(C/D)
24	1.4 M LiDFP-G4/HFE	NCM523‖Li (1000 μm)	4.5 V 98.5%@100 cycles, 0.5 C, N/P=100.5	-60 °C 42.0%@0.1 C (charged at RT)	60 °C 81.0%@200 cycles, 0.5 C/1 C (C/D)
25	1 M LiPF$_6$-FEC/BTC (3:7 by vol.)	NCM811‖Li (450/50 μm)	4.8 V 81.3%@120 cycles, 0.5 C, N/P=5	-30 °C 64%@0.1 C	55 °C 80%@149 cycles, 0.5 C
26	1 M LiFSI-BEF	NCM811‖Li (400/50/40 μm)	4.4 V ＞90%@200 cycles, 2 C, N/P=2.8	-60 °C ~45%@0.1 C	60 °C @0.1 C
27	LiDFOB/TEP/HFE (1/2.5/2 by mol.)	NCM523‖Li	4.5 V 98.2%@200 cycles, 0.5 C, N/P=5	-40 °C 50%@0.05 C	70 °C 93.2%@100 cycles, 0.5 C
28	LiTFSI/LiDFOB/DME /TTE (0.5/0.5/1.8/9)	NCM523‖Li (N/P=0.9)	4.5 V 70%@175 cycles, 1 C, N/P=0.9	-40 °C 71%@0.1 C (charged at RT)	80 °C 85%@200 cycles, 1 C
29	LiFSI/TMS/FB/TFB (1/3/2.333/0.167 by mol.)	NCM811‖Li (50 μm)	4.5 V 83.0%@100 cycles, 0.5 C, N/P=2.86	-20 °C 67.6%@0.2 C	60 °C 86.8%@200 cycles, 1 C, 4.3 V
30	1 mol/kg LiFSI+0.2 mol/kg LiNO$_3$-MODOL	LFP‖Li (N/P=2.5 or 4)	3.85 V 83%@150 cycles, 1 C, N/P=2.5	-20 °C ~59%@0.2 C	50 °C 80%@90 cycles, 0.5 C, 4.3 V, N/P=4
31	0.5 M LiDFOB/0.2 M LiPO$_2$F$_2$/0.3 M LiPF$_6$-EMC/DMC (7:3 by vol.)	NCM811‖Li (100 μm)	4.7 V ＞80%@500 cycles, 1 C, N/P=25.8	-30 °C ~65%@0.2 C	45 °C ~80%@200 cycles, 1 C, 4.7 V
32	1 M LiPF$_6$-FEC/ETFB (1:4 by vol.)	LCO‖Li (200 μm)	4.5 V 91.9%@200 cycles, 0.2 C, N/P~24	-60 °C 66.7%@0.1 C (charged at RT)	70 °C 85.9%@100 cycles, 0.5 C, 4.5 V
This work	1 M LiPF$_6$ -FEMC/FEC/MA (4:2:4 by vol.)	NCM811‖Li (N/P=2 in coin cell, N/P~3.4 in pouch cell)	4.8 V 92.5%/74.4% @100/200 cycles, 5 C, N/P=2	-70 °C 65.2%/40.8% (159.1/99.1 mAh g^{-1}) @0.05/0.1 C (charged at RT)	60 °C 79.4%@100 cycles, 5 C, 4.5 V
			4.5 V (1 Ah pouch cell) X% @100 cycles, 0.2 A, N/P~3.4	-40/-50/-60 °C 61.6%/56.35/35.0% (150.3/137.3/85.3 mAh g^{-1})@0.1 C	

Note:

The following lists the full names of the reagents mentioned in the table:

LiCoO$_2$ (LCO)

LiNi$_{0.5}$Co$_{0.2}$Mn$_{0.3}$O$_2$ (NCM523)

LiNi$_{0.8}$Co$_{0.1}$Mn$_{0.1}$O$_2$ (NCM811)

Lithium bis(fluorosulfonyl)imide (LiFSI)

Lithium difluorophosphate ($LiPO_2F_2$)
Lithium hexafluorophosphate ($LiPF_6$)
Lithium difluoro(oxalato)borate (LiDFOB)
Lithium bis(trifluoromethanesulfonyl) (LiTFSI)
1,2-Dimethoxyethane (DME)
1,1,2,2-Tetrafluoroethyl 2,2,3,3-tetrafluoropropyl ether (TTE)
Tetraglyme (G4)
Fluoroethylene carbonate (FEC)
Bis(2,2,2-trifluoroethyl) carbonate (BTC)
Bis(2-fluor-oethyl) ethers (BFE)
Triethyl phosphate (TEP)
Tetramethylene sulfone (TMS)
Fluorobenzene (FB)
1,3,5-Trifluorobenzene (TFB)
2-Methoxy-1,3-dioxolane (MODOL)
Dimethyl carbonate (DMC)
Methyl ethyl carbonate (EMC)
4,4,4-Trifluorobutyrate (ETFB)

References

1 T. Lu and F. Chen, *J. Comput. Chem.*, 2011, **33**, 580–592.

2 T. Lu, *J. Chem. Phys.*, 2024, **161**, 082503.

3 J. Zhang and T. Lu, *Phys. Chem. Chem. Phys.*, 2021, **23**, 20323–20328.

4 W. Cai, Y. Deng, Z. Deng, Y. Jia, Z. Li, X. Zhang, C. Xu, X. Q. Zhang, Y. Zhang and Q. Zhang, *Adv. Energy Mater.*, 2023, **13**, 2301396.

5 L. Su, E. Jo and A. Manthiram, *ACS Energy Lett.*, 2022, **7**, 2165–2172.

6 T. N. Tran, X. Cao, Y. Xu, P. Gao, H. Zhou, F. Guo, K. S. Han, D. Liu, P. M. L. Le, J. M. Weller, M. H. Engelhard, C. Wang, M. S. Whittingham, W. Xu and J. G. Zhang, *Adv. Funct. Mater.*, 2024, **34**, 2407012.

7 L. Xu, J. Yang, M. Huang, L. Pi, K. Du, D. Wang, A. Lin and C. Peng, *Chem. Eng. J.*, 2021, **419**, 129494.

8 Z. Guo, M. Yang, Q. Fan, Y. Chen, T. Xu, C. Li, Z. Li, Z. Li, Q. Sun and H. Xia, *Small*, 2024, **20**, 2407425.

9 G. M. Hobold, C. Wang, K. Steinberg, Y. Li and B. M. Gallant, *Nat. Energy*, 2024, **9**, 580–591.

10 A. Einstein, *Ann. Phys.*, 1905, **322**, 549–560.

11 J. Quirk, M. Rothmann, W. Li, D. Abou-Ras and K. P. McKenna, *Appl. Phys. Rev.*, 2024, **11**, 011308.

12 E. R. Logan, E. M. Tonita, K. L. Gering, J. Li, X. Ma, L. Y. Beaulieu and J. R. Dahn, *J. Electrochem. Soc.*, 2018, **165**, A21–A30.

13 Q. Li, G. Liu, H. Cheng, Q. Sun, J. Zhang and J. Ming, *Chem. Eur. J.*, 2021, **27**, 15842–15865.

14 Laurence Christian and J.-F. Gal, *Lewis basicity and affinity scales: data and measurement*, John Wiley & Sons, 2009.

15 Z. Hong, H. Tian, Z. Fang, Y. Luo, H. Wu, F. Zhao, Q. Li, S. Fan and J. Wang, *ChemElectroChem*, 2024, **11**, e202300759.

16 N. von Aspern, G. V. Röschenthaler, M. Winter and I. Cekic-Laskovic, *Angew. Chemie - Int. Ed.*, 2019, **58**, 15978–16000.

17 M. Takehara, S. Watanabe, N. Nanbu, M. Ue and Y. Sasaki, *Synth. Commun.*, 2004, **34**, 1367–1375.

18 S. Tan, O. Borodin, N. Wang, D. Yen, C. Weiland and E. Hu, *J. Am. Chem. Soc.*, 2024, **146**, 30104–30116.

19 SutingWeng, X. Zhang, G. Yang, S. Zhang, B. Ma, Q. Liu, Y. Liu, C. Peng, H. Chen, H. Yu, X. Fan, T. Cheng, L. Chen, Y. Li, Z. Wang and X. Wang, *Nat. Commun.*, 2023, **14**, 4474.

20 J. Xu, J. Zhang, T. P. Pollard, Q. Li, S. Tan, S. Hou, H. Wan, F. Chen, H. He, E. Hu, K. Xu, X.-Q. Yang, O. Borodin and C. Wang, *Nature*, 2023, **614**, 694–700.

21 J. Holoubek, M. Yu, S. Yu, M. Li, Z. Wu, D. Xia, P. Bhaladhare, M. S. Gonzalez, T. A. Pascal, P. Liu and Z. Chen, *ACS Energy Lett.*, 2020, **5**, 1438–1447.

22 Y. Huang, R. Li, S. Weng, H. Zhang, C. Zhu, D. Lu, C. Sun, X. Huang, T. Deng, L. Fan, L. Chen, X. Wang and X. Fan, *Energy Environ. Sci.*, 2022, **15**, 4349–4361.

23 X. Ren, X. Zhang, Z. Shadike, L. Zou, H. Jia, X. Cao, M. H. Engelhard, B. E. Matthews, C. Wang, B. W. Arey, X. Q. Yang, J. Liu, J. G. Zhang and W. Xu, *Adv. Mater.*, 2020, **32**, 2004898.

24 S. Kuang, H. Hua, P. Lai, J. Li, X. Deng, Y. Yang and J. Zhao, *ACS Appl. Mater. Interfaces*, 2022, **14**, 19056–19066.

25 P. Xiao, Y. Zhao, Z. Piao, B. Li, G. Zhou and H. M. Cheng, *Energy Environ. Sci.*, 2022, **15**,

2435–2444.

26 G. Zhang, J. Chang, L. Wang, J. Li, C. Wang, R. Wang, G. Shi, K. Yu, W. Huang, H. Zheng, T. Wu, Y. Deng and J. Lu, *Nat. Commun.*, 2023, **14**, 1081.

27 W. N. Cbuufsjft, A. Pan, Z. Wang, F. Zhang, L. Wang, J. Xu, ㅎ J. Z. and J. Hu, *Nano Res.*, 2023, **16**, 8260–8268.

28 J. Li, H. Hua, X. Deng, P. Lai, Y. Kang, S. Kuang, F. Wang, X. Zeng, Y. Zhang and J. Zhao, *Chem. Eng. J.*, 2023, **452**, 139398.

29 R. He, Q. Zhang, Y. Hu, H. Xie, C. Y. Li, Z. Yan, K. Yang and K. Deng, *Energy Storage Mater.*, 2024, **73**, 103836.

30 X. Zhu, J. Chen, G. Liu, Y. Mo, Y. Xie, K. Zhou, Y. Wang and X. Dong, *Angew. Chemie Int. Ed.*, 2024, **64**, e202412859.

31 F. Cheng, W. Zhang, Q. Li, C. Fang, J. Han and Y. Huang, *ACS Nano*, 2023, **17**, 24259–24267.

32 C. Chen, S. Zhang, C. Xu, J. Yang, Y. Hu, L. Yu, P. Li, B. Qu and M. Wu, *J. Energy Chem.*, 2025, **101**, 608–618.